Guided wave propagation in buried and immersed fluid-filled pipes:

application of the semi analytic finite element method

Wenbo Duan[a], Ray Kirby[b*]

[a] *Department of Mechanical, Aerospace and Civil Engineering, Brunel University London, Uxbridge, Middlesex, UK, UB8 3PH*

[b]*Centre for Audio, Acoustics and Vibration, University of Technology, Sydney, NSW, 2007, Australia.*

* Corresponding author.

ABSTRACT

Developing an understanding of guided wave propagation in multi-layered systems has important applications in non-destructive evaluation. This article presents a general weighted residual formulation for guided wave propagation in fluid-filled pipes buried in an elastic solid, or immersed in a quiescent fluid. A one-dimensional semi-analytic finite element (SAFE) approach is combined with a perfectly matched layer (PML), to compute dispersion curves for different pipe applications. The speed and accuracy of this approach are compared against the scaled boundary finite element method (SBFEM) and it is shown that for a rod immersed in a liquid the two methods provide very similar computational speeds. The speed and accuracy of the model is then investigated for immersed and buried fluid-filled pipes, and it is shown that when discretising the PML no advantage in computational speed is found when using either quadratic or higher order spectral elements, provided the number of degrees of freedom in the PML is equivalent. Accordingly, it is shown that the SAFE-PML method is capable of obtaining accurately the modal characteristics of buried and immersed fluid-filled pipes, with computational speeds comparable to the SBFEM approach.

Key words: SAFE-PML method; Buried pipes; Immersed pipes; Waveguide energy distribution; Spectral elements.

1. Introduction

The propagation of elastic waves along the walls of pipelines plays an important role in the detection of leaks and the identification of defects such as cracks or regions of corrosion. For example, non-destructive testing often makes use of propagating elastic waves to identify the presence of defects, and this is normally carried out in the ultrasonic frequency range [1]. Alternatively, if pipelines are filled with a liquid, then ruptures of the wall can generate acoustic waves in the low audio frequency range, which can then be detected by remote monitoring equipment placed in the fluid or on the walls [2, 3]. These detection techniques rely on the propagation of acoustic energy in both the structure and the fluid, as well as the detection and interpretation of energy transfer. However, it is common for these pipelines also to be buried underground, or immersed in a fluid, and this can significantly affect the propagation of energy. This often leads to a reduction in the effectiveness of detection techniques and so it is important to develop a good understanding of the physics underpinning this wave propagation if one is to develop reliable inspection methodologies.

Analytic methods are available to analyse this type of problem and the commercial available software DISPERSE is capable of obtaining the low order modes for buried pipes. For example, Aristégui et al [4] and Leniov et al. [5, 6] use DISPERSE to obtain torsional and longitudinal modes for a pipe immersed in fluids or buried in sand, and generally good agreement is obtained with experimental measurements for axisymmetric modes. However, an analytic solution is difficult to undertake for complex problems where large numbers of modes are present, and so it is convenient to use numerical methods and the analysis of pipes and cylinders or rods is now well established [7-11]. However, if the pipe is buried in an elastic solid, or immersed in a liquid, then one must address the challenge of capturing the sound field in the surrounding (nominally infinite) domain. If one adopts a finite element based approximation then it is necessary to close the problem so that the mesh is restricted to a finite outer region,

but at the same time one also needs to enforce the appropriate radiation boundary conditions at infinity. For solutions in the frequency domain, this complexity has led to the semi analytic finite element (SAFE) method being favoured, with a surrounding absorbing layer used to damp down outward propagating waves. Relevant examples include the study of an immersed bar by Fan et al. [12], and a buried structure of arbitrary cross-section by Castaings and Lowe [13]. Recently, an alternative to absorbing layers was proposed by Nguyen et al. [14], who showed that a perfectly matched layer (PML) is more numerically efficient than an equivalent absorbing layer for an elastic waveguide of arbitrary cross-section buried in an infinite elastic medium. Zuo and Fan recently applied a similar approach for an elastic waveguide immersed in a fluid [15]. If one is interested in axisymmetric geometries such as pipes or rods, Duan et al. [16] also showed that for buried pipes the axisymmetric problem can readily be reduced from two to one dimension, and a relatively thin PML can be attached directly to the outer surface of the pipe. This significantly lowers the number of degrees of freedom required and delivers significant improvements in the computational speed of a SAFE-PML based approach. Matuzzyk [17] also demonstrated the efficiency of a one dimensional finite element based approach, although this analysis is restricted to propagation in the circumferential direction only. Kalkowski et al. [18] recently used a variational formulation to examine buried and submerged fluid filled pipes using a SAFE-PML approach with spectral finite elements.

Thus, recent articles illustrate that one may significantly improve the speed of a SAFE-PML approach, however this approach requires a PML and this generates its own non-physical eigensolutions. This means that one must sort so-called trapped and leaky modes from radiation type modes when adopting the SAFE-PML method. Nguyen et al. [14] showed how this sorting can be done by comparing the average kinetic energy in each region, however this adds a further computational expense. This has motivated attempts to try and find alternatives, and Hua et al. [19] use infinite elements over the outer surface of the waveguide. Hua et al.

developed an efficient one-dimensional solution for an axisymmetric problem and applied this approach to the analysis of buried pipes. However, this method requires the generation of new FE basis functions that are known to be computationally unstable in regions of high modal densities [20]. Hlasky-Hennison et al. [21] adopted a similar approach, this time using so-called radiating elements for the outer surface of their FE mesh, and applied this to wave propagation in an immersed solid structure. However, this approach requires the outer surface of the FE domain to be in the acoustic far field of the solid structure, which is likely to require a large outer domain and so will be computationally efficient only for low order modes and lower frequencies. To completely remove the discretisation of the outer region, Mazzotti et al. [22-24] proposed coupling a SAFE formulation for the internal solid structure to a boundary integral formulation for the exterior region. Application of the boundary element method then reduces the discretisation of the exterior domain to the outer surface of the guide only, which avoids problems associated with meshing a finite outer region. Recently, Gravenkamp et al. [25-27] proposed the use of the scaled boundary finite element method (SBFEM), which uses an analytic formulation to scale this exterior domain. The Sommerfeld radiation condition is then enforced by placing numerical dashpots on the outer surface of the guide, although an exact dashpot boundary condition only exists for a fluid exterior domain, and so for an elastic exterior the solution is only approximate. This method has been applied by Gravenkamp et al. to one and two dimensional problems [25-27], and fast solution times are shown to be possible. Furthermore, this method does not require one to sort and remove those radiation type modes typically found when using a PML based method, which further helps to speed up the method.

The method presented by Gravekamp et al. [25] delivers fast and accurate solutions and so this method presents a benchmark for this particular type of problem, at least for an immersed waveguide. Accordingly, this article will compare the SAFE-PML approach against predictions obtained using the SBFEM method of Gravekamp et al. This comparison will make

use of an optimised version of the general weighted residual method that has not previously been reported for the SAFE-PML approach. This is important because identifying a general FE based approach that is at least comparable in speed and accuracy to the SBFEM approach means that one can continue to take advantage of standard FE codes. Of course, the trade-off with the SAFE-PML approach is that one has to mesh an outer layer and identify and remove the radiation modes, and so this trade-off between the two methods is also explored here. Furthermore, recent developments of the SAFE-PML method have introduced the use of spectral elements [18] and so this article will also investigate if spectral elements provide any computational advantages in terms of solution speed and accuracy when compared to the quadratic finite elements used by Duan et al. [16]. The investigation extends to both buried and immersed fluid filled pipelines because these represent common applications, and so in section 2 the weighted residual method is used to develop a new version of the SAFE-PML approach for fluid filled pipes; this is then benchmarked for an immersed rod in section 3, and extended to the more challenging problems of an immersed and buried fluid-filled pipes in sections 4 and 5. In section 6, material damping is added to the outer region, and conclusions are drawn in section 7.

2. Theory

In this section the weighted residual method is applied to a fluid-filled pipe that consists of a number of elastic or viscoelastic layers, although each layer is assumed here to be homogenous and isotropic. The weighted residual method is adopted here because of its generality and this method is re-cast here to enable frequency independent matrices to be assembled, which provides the weighted residual alternative to the variational approach by Kalkowski et al. [18]. Accordingly, the pipe is assumed to be surrounded by an infinite medium so that it is either buried in a solid elastic structure, or immersed in a quiescent fluid. This is illustrated in Fig. 1, where the layer Ω_0 represents the internal fluid, layers Ω_j, for $j =$

$1, \ldots, m-1$, denote the [elastic] pipe layers, and Ω_m is the outer region where a PML is applied, which is either a fluid or an elastic solid.
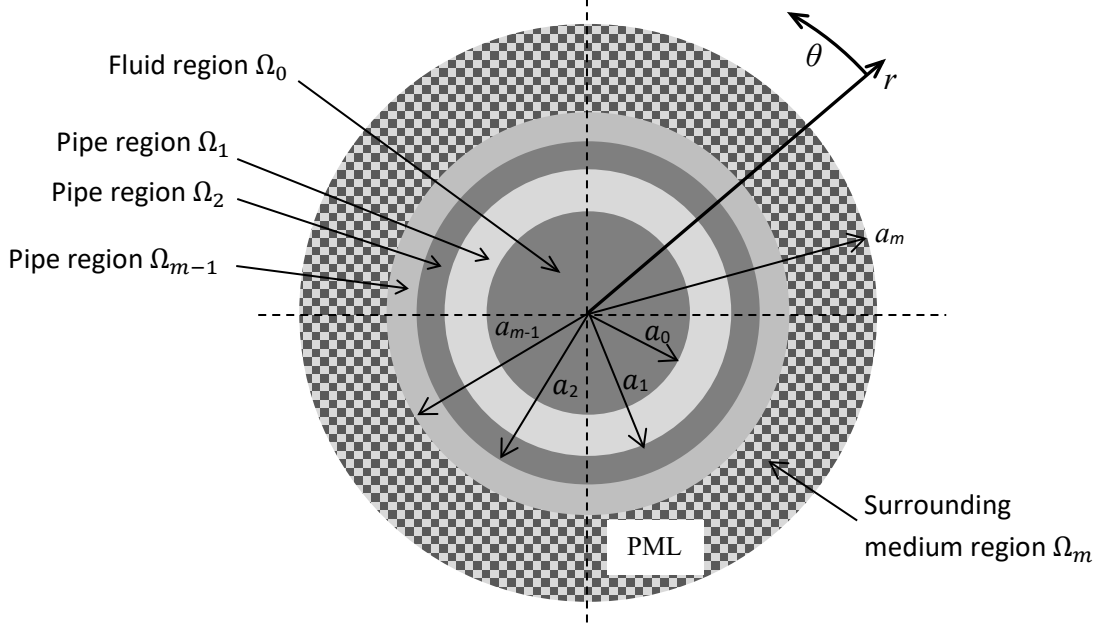

Figure 1. Geometry of fluid-filled pipe.

2.1. *Governing Equations for Elastic Region*

The one dimensional form of Navier's elastodynamic equations in cylindrical co-ordinates for layer Ω_j $(j = 1 \text{ to } m-1)$ gives [16]

$$\rho_j \frac{\partial^2 u'_{r_j}}{\partial t^2} = \frac{\partial \sigma'_{rr_j}}{\partial r} + \frac{1}{r}\frac{\partial \sigma'_{r\theta_j}}{\partial \theta} + \frac{\partial \sigma'_{rz_j}}{\partial z} + \frac{1}{r}\left(\sigma'_{rr_j} - \sigma'_{\theta\theta_j}\right) \tag{1}$$

$$\rho_j \frac{\partial^2 u'_{\theta_j}}{\partial t^2} = \frac{\partial \sigma'_{\theta r_j}}{\partial r} + \frac{1}{r}\frac{\partial \sigma'_{\theta\theta_j}}{\partial \theta} + \frac{\partial \sigma'_{\theta z_j}}{\partial z} + \frac{2}{r}\sigma'_{r\theta_j} \tag{2}$$

$$\rho_j \frac{\partial^2 u'_{z_j}}{\partial t^2} = \frac{\partial \sigma'_{zr_j}}{\partial r} + \frac{1}{r}\frac{\partial \sigma'_{z\theta_j}}{\partial \theta} + \frac{\partial \sigma'_{zz_j}}{\partial z} + \frac{1}{r}\sigma'_{rz_j} \tag{3}$$

where r, θ and z form an orthogonal cylindrical co-ordinate system in the radial, circumferential and axial directions of the waveguide, respectively, see Fig. 1. In addition, ρ is density, t is time, u' is displacement and σ'_{ql} ($q, l = r, \theta$ or z) is the stress tensor. A time

dependence of $e^{i\omega t}$ is assumed throughout this article, where ω is the radian frequency and $i = \sqrt{-1}$. The displacement sound field is assumed to be harmonic in the circumferential direction, and the coupled displacement u' for all layers is expanded in the form

$$u'_q(r) = u_q(r)e^{i[\omega t - n\theta - k_{T_1}\gamma z]}, \tag{4}$$

where u_q is an eigenfunction ($q = r, \theta$ or z), and γ is a dimensionless wavenumber. In addition, n denotes circumferential mode order, $k_{T_1} = \omega/c_{T_1}$, and c_{T_1} and c_{L_1} are the shear (torsional) and compressional (longitudinal) bulk wave velocities for (elastic) layer Ω_1, respectively. The weighted residual method is used and so Eqs. (1)-(3) are weighted using the arbitrary function w_q. The weak forms of Eqs. (1) to (3) are then obtained by making use of the usual relationships between stress and strain [16]. Layers from Ω_1 to Ω_{m-1} are combined by enforcing continuity of displacement and normal shear stress over the interface between each layer. Three equations for the elastic regions are delivered by setting $\zeta = ik_{T_1}\gamma$ and $\tilde{\mathbf{u}}_\theta = i\mathbf{u}_\theta$:

$$\mathbf{R}_{10}\mathbf{u_r} - \zeta^2\mathbf{R}_{12}\mathbf{u}_r + \mathbf{\Theta}_{10}\tilde{\mathbf{u}}_\theta + \zeta\mathbf{Z}_{11}\mathbf{u}_z = w_r\sigma_{rr_{m-1}}\big|_{r=a_{m-1}} - w_r\sigma_{rr_1}\big|_{r=a_0} \tag{5}$$

$$\mathbf{\Theta}_{20}\tilde{\mathbf{u}}_\theta - \zeta^2\mathbf{\Theta}_{22}\tilde{\mathbf{u}}_\theta + \mathbf{R}_{20}\mathbf{u_r} + \zeta\mathbf{Z}_{21}\mathbf{u}_z = w_\theta\sigma_{\theta r_{m-1}}\big|_{r=a_{m-1}} - w_\theta\sigma_{\theta r_1}\big|_{r=a_0} \tag{6}$$

$$\mathbf{Z}_{30}\mathbf{u}_z - \zeta^2\mathbf{Z}_{32}\mathbf{u}_z + \zeta\mathbf{R}_{31}\mathbf{u}_r + \zeta\mathbf{\Theta}_{31}\tilde{\mathbf{u}}_\theta = w_z\sigma_{zr_{m-1}}\big|_{r=a_{m-1}} - w_z\sigma_{zr_1}\big|_{r=a_0} \tag{7}$$

The matrices that make up these equations are listed in Appendix A, and the Lamé constants are given by λ and μ; the vectors for displacement contain the individual displacements in each layer, so that $\mathbf{u}_q = [\mathbf{u}_{q1} \quad \mathbf{u}_{q2} \quad \cdots \quad \mathbf{u}_{q(m-1)}]$.

2.2. *Governing Equations for the Inner Fluid Region*

The appropriate wave equation for the fluid layer Ω_0 is Helmholtz's equation, which in cylindrical co-ordinates gives

$$\frac{\partial^2 p_0'}{\partial r^2} + \frac{1}{r}\frac{\partial p_0'}{\partial r} + \frac{1}{r^2}\frac{\partial^2 p_0'}{\partial \theta^2} + \frac{\partial^2 p_0'}{\partial z^2} - \frac{1}{c_0^2}\frac{\partial^2 p_0'}{\partial t^2} = 0, \tag{8}$$

where p_0' is the acoustic pressure and c_0 is the speed of sound in the fluid, layer Ω_0. The ansatz for pressure is the same as for the displacement in the structure, so that

$$p_0'(r) = p_0(r)e^{i\left[\omega t - n\theta - k_{T_1}\gamma z\right]}. \tag{9}$$

Adopting the weighted residual method yields the following eigenequation:

$$\mathbf{R}_{00}\tilde{\mathbf{p}}_0 - \zeta^2 \mathbf{R}_{20}\tilde{\mathbf{p}}_0 = \frac{1}{\rho_0 \omega^2} w_0 \left.\frac{\partial p_0}{\partial r}\right|_{r=a_0} \tag{10}$$

where w_0 is the weighting function, and $k_0 = \omega/c_0$. The pressure is non-dimensionalised so that $\rho_0 \omega^2 \tilde{\mathbf{p}}_0 = \mathbf{p}_0$, and ρ_0 is the fluid density in region Ω_0; the matrices in Eq. (10) can be found in Appendix B. To solve the fluid-filled pipe problem, it is necessary to couple together each layer and this is done separately for the case of a solid or a fluid in the outer layer.

2.3. *A SAFE-PML model for fluid-filled buried pipes*

A fluid-filled buried pipe is analysed first, and this requires Eqs. (5)-(7) and Eq. (10) to be coupled together. A PML is also used to model layer Ω_m, and the stretching function is specified here as

$$\tilde{r} = \int_0^r \xi(s)ds, \tag{11}$$

where ξ is a non-zero, continuous and complex-valued coordinate stretching function. To couple the inner fluid and the pipe layers together it is necessary to apply the appropriate boundary conditions at the interface $r = a_0$, which gives

$$\frac{1}{\rho_0 \omega^2} \frac{\partial p}{\partial r} = u_r \quad \text{and} \quad p = -\sigma_{rr}. \tag{12a,b}$$

The boundary condition given by Eq. (12a) is substituted into the right hand side of Eq. (10), and Eq. (12b) is substituted into the right hand side of Eq. (5). In addition, zero traction in the circumferential and axial directions is applied at $r = a_0$, and at the exterior of the PML zero traction is also applied. This latter condition is used because it provides a convenient simplification of the governing equations. The variable ξ is then chosen to deliver an efficient PML and this is discussed in sections 3 and 4. Following the application of these boundary conditions, Eqs. (5)-(7) and Eq. (10) are combined to yield the following eigenequation

$$\begin{bmatrix} \mathbf{Z} & \mathbf{0} \\ \mathbf{0} & \mathbf{X}^T \end{bmatrix} \begin{Bmatrix} \mathbf{L} \\ \zeta \mathbf{L} \end{Bmatrix} = \zeta \begin{bmatrix} \mathbf{Y} & \mathbf{X} \\ \mathbf{X}^T & \mathbf{0} \end{bmatrix} \begin{Bmatrix} \mathbf{L} \\ \zeta \mathbf{L} \end{Bmatrix} \tag{13}$$

where $\mathbf{L} = [\tilde{\mathbf{p}}_0 \quad \mathbf{u}_r \quad \tilde{\mathbf{u}}_\theta \quad \mathbf{u}_z]$, and $\mathbf{u}_q$ includes displacements in the outer PML layer Ω_m. In addition,

$$\mathbf{Z} = \begin{bmatrix} \mathbf{R}_{00} & -\mathbf{C}_{01} & \mathbf{0} & \mathbf{0} \\ -\mathbf{C}_{10} & \mathbf{R}_{10} & \mathbf{\Theta}_{10} & \mathbf{0} \\ \mathbf{0} & \mathbf{R}_{20} & \mathbf{\Theta}_{20} & \mathbf{0} \\ \mathbf{0} & \mathbf{0} & \mathbf{0} & \mathbf{Z}_{30} \end{bmatrix} \tag{14}$$

$$\mathbf{Y} = \begin{bmatrix} \mathbf{0} & \mathbf{0} & \mathbf{0} & \mathbf{0} \\ \mathbf{0} & \mathbf{0} & \mathbf{0} & -\mathbf{Z}_{11} \\ \mathbf{0} & \mathbf{0} & \mathbf{0} & -\mathbf{Z}_{21} \\ \mathbf{0} & -\mathbf{R}_{31} & -\mathbf{\Theta}_{31} & \mathbf{0} \end{bmatrix} \tag{15}$$

$$\mathbf{X} = \begin{bmatrix} \mathbf{R}_{20} & \mathbf{0} & \mathbf{0} & \mathbf{0} \\ \mathbf{0} & \mathbf{R}_{12} & \mathbf{0} & \mathbf{0} \\ \mathbf{0} & \mathbf{0} & \mathbf{\Theta}_{22} & \mathbf{0} \\ \mathbf{0} & \mathbf{0} & \mathbf{0} & \mathbf{Z}_{32} \end{bmatrix}. \tag{16}$$

10

The matrices that couple together the fluid and elastic layers are given as

$$\mathbf{C}_{01} = \mathbf{W}_0^{\mathrm{T}}\mathbf{N}\big|_{r=a_0} \quad \text{and} \quad \mathbf{C}_{10} = \rho_m \omega^2 \mathbf{W}^{\mathrm{T}}\mathbf{N}\big|_{r=a_0} \tag{17a,b}$$

Equation (13) is an eigenequation and solution of this equation will deliver an unordered list of $N_T = 2(N_p + 3N_u)$ eigenmodes, where N_p is the number of nodes in the fluid, and N_u is the total number of nodes in the pipe and the PML layers. Note that all of the matrices that populate Eq. (13), apart from $\mathbf{R}_{00}$ and $\mathbf{M}_7$ are frequency independent if the material properties are themselves frequency independent. This does of course help to speed up the computation of dispersion curves.

2.4. *A SAFE model for fluid-filled immersed pipes*

For a fluid-filled immersed pipe, Eqs. (5)-(7) and Eq. (10) are coupled together in the same way as in the previous section, however this time the integral over the PML region (Ω_m) in Eqs. (A7) to (A19) is removed and replaced with a fluid in the outer region. Accordingly, Helmholtz's equation in the outer layer, Ω_m, is recast by replacing the radial coordinate r with $\tilde{r}$, and this delivers:

$$\frac{1}{\xi}\frac{\partial}{\partial r}\left(\frac{1}{\xi}\frac{\partial p_m'}{\partial r}\right) + \frac{1}{\xi}\frac{1}{\tilde{r}}\frac{\partial p_m'}{\partial r} + \frac{1}{\tilde{r}^2}\frac{\partial^2 p_m'}{\partial \theta^2} + \frac{\partial^2 p_m'}{\partial z^2} - \frac{1}{c_m^2}\frac{\partial^2 p_m'}{\partial t^2} = 0 \tag{18}$$

Here, c_m is the speed of sound in the outer fluid layer (Ω_m). Multiplying Eq. (18) by ξ and applying the arbitrary weighting function w_m, yields the following weak form:

$$\int_{\Omega_m}\left(\frac{1}{\xi}\frac{\partial w_m}{\partial r}\frac{\partial p_m'}{\partial r} - \frac{1}{\tilde{r}}w_m\frac{\partial p_m'}{\partial r} - \xi\frac{1}{\tilde{r}^2}w_m\frac{\partial^2 p_m'}{\partial \theta^2} - \xi w_m\frac{\partial^2 p_m'}{\partial z^2} + \xi\frac{1}{c_m^2}w_m\frac{\partial^2 p_m'}{\partial t^2}\right)dr$$
$$= w_m\frac{1}{\xi}\frac{\partial p_m'}{\partial r}\bigg|_{r=a_{m-1}}^{r=a_m} \tag{19}$$

In the matrix form, this gives

$$\mathbf{R}_{0m}\tilde{\mathbf{p}}_m - \zeta^2\mathbf{R}_{2m}\tilde{\mathbf{p}}_m = \frac{1}{\rho_m\omega^2}w_m\frac{1}{\xi}\frac{\partial p_m}{\partial r}\bigg|_{r=a_{m-1}}^{r=a_m} \tag{20}$$

The boundary conditions in Eqs. (12a,b) apply also to the interface at $r = a_{m-1}$, and zero

traction at the exterior of the PML is now replaced with zero normal velocity. Following the

application of these boundary conditions, the global eigenequation can be assembled in the

same form as Eq. (13), so that

$$
\mathbf{Z} = \begin{bmatrix}
\mathbf{R}_{00} & -\mathbf{C}_{01} & \mathbf{0} & \mathbf{0} & \mathbf{0} \\
-\mathbf{C}_{10} & \mathbf{R}_{10} & \mathbf{\Theta}_{10} & \mathbf{0} & \mathbf{C}_{1m} \\
\mathbf{0} & \mathbf{R}_{20} & \mathbf{\Theta}_{20} & \mathbf{0} & \mathbf{0} \\
\mathbf{0} & \mathbf{0} & \mathbf{0} & \mathbf{Z}_{30} & \mathbf{0} \\
\mathbf{0} & \mathbf{C}_{m1} & \mathbf{0} & \mathbf{0} & \mathbf{R}_{0m}
\end{bmatrix}
\tag{21}
$$

$$
\mathbf{Y} = \begin{bmatrix}
\mathbf{0} & \mathbf{0} & \mathbf{0} & \mathbf{0} & \mathbf{0} \\
\mathbf{0} & \mathbf{0} & \mathbf{0} & -\mathbf{Z}_{11} & \mathbf{0} \\
\mathbf{0} & \mathbf{0} & \mathbf{0} & -\mathbf{Z}_{21} & \mathbf{0} \\
\mathbf{0} & -\mathbf{R}_{31} & -\mathbf{\Theta}_{31} & \mathbf{0} & \mathbf{0} \\
\mathbf{0} & \mathbf{0} & \mathbf{0} & \mathbf{0} & \mathbf{0}
\end{bmatrix}
\tag{22}
$$

$$
\mathbf{X} = \begin{bmatrix}
\mathbf{R}_{20} & \mathbf{0} & \mathbf{0} & \mathbf{0} & \mathbf{0} \\
\mathbf{0} & \mathbf{R}_{12} & \mathbf{0} & \mathbf{0} & \mathbf{0} \\
\mathbf{0} & \mathbf{0} & \mathbf{\Theta}_{22} & \mathbf{0} & \mathbf{0} \\
\mathbf{0} & \mathbf{0} & \mathbf{0} & \mathbf{Z}_{32} & \mathbf{0} \\
\mathbf{0} & \mathbf{0} & \mathbf{0} & \mathbf{0} & \mathbf{R}_{2m}
\end{bmatrix}
\tag{23}
$$

where $\mathbf{L} = [\widetilde{\mathbf{p}}_0 \quad \mathbf{u_r} \quad \widetilde{\mathbf{u}}_\theta \quad \mathbf{u}_z \quad \widetilde{\mathbf{p}}_m]$, and

$$
\mathbf{C}_{m1} = \mathbf{W}_m^{\mathrm{T}}\mathbf{N}\big|_{r=a_0} \quad \text{and} \quad \mathbf{C}_{1m} = \rho_m \omega^2 \mathbf{W}_m^{\mathrm{T}}\mathbf{N}\big|_{r=a_{m-1}}.
\tag{24a,b}
$$

For this problem, the solution delivers an unordered list of $N_T = 2(N_p + 3N_u)$

eigenmodes, where N_p is the number of nodes in the fluid region Ω_0 and the PML region Ω_m,

and N_u is the total number of nodes in the pipe and any additional layers (but does not

include the PML).

2.5. *Computing dispersion curves and energy distribution*

The eigenproblem is solved using a one-dimensional finite element mesh and the

eigensolver 'eig' in MATLAB®. This is executed in this study using a laptop with four 2.6 GHz

Intel Core™ CPU processors and 16 GB of RAM. The phase velocity (c_p) and the

attenuation (Δ) for an individual mode are given as

$$c_p = \omega/\text{Re}(-i\zeta) \qquad \text{and} \qquad \Delta = 8.686\,\text{Im}(i\zeta) \qquad (25a,b)$$

The eigensolution yields an unordered list of eigenvalues and associated eigenvectors and

these are identified and sorted using the method described by Nguyen et al. [14], which sorts

according to the balance between the average kinetic energy over the cross section of each

layer, Ω_j, for each eigenmode. This enables separation of the radiation from leaky and

trapped modes and here the average kinetic energy in an elastic region is given as

$$K_j = \frac{\pi}{2}\int_{\Omega_j} \rho_j \omega^2 \text{Re}[\mathbf{u}_j^* \cdot \mathbf{u}_j]\text{Re}(\xi)\text{Re}(\tilde{r})dr \qquad j = 1 \text{ to } m \qquad (26)$$

where, $\tilde{r} = r$ and $\xi = 1$ for $j = 1, m-1$, and Eq. (26) applies for $j = m$ if the exterior

region Ω_m is elastic. For a fluid region, the average kinetic energy, is

$$K_j = \frac{\pi}{2}\int_{\Omega_j} \rho_j \omega^2 \text{Re}\left[\frac{1}{\xi^*}\frac{\partial \widetilde{\mathbf{p}}_j^*}{\partial r} \cdot \frac{1}{\xi}\frac{\partial \widetilde{\mathbf{p}}_j}{\partial r} + n^2 \frac{1}{\tilde{r}^*}\widetilde{\mathbf{p}}_j^* \cdot \frac{1}{\tilde{r}}\widetilde{\mathbf{p}}_j + \zeta^*\widetilde{\mathbf{p}}_j^* \cdot \zeta\widetilde{\mathbf{p}}_j\right]\text{Re}(\xi)\text{Re}(\tilde{r})dr,$$
$$j = 0, \text{ or } m, \qquad (27)$$

where, $\tilde{r} = r$ and $\xi = 1$ for $j = 0$, and Eq. (27) applies for $j = m$ if the exterior region Ω_m

is a fluid. The ratio of the kinetic energy in PML to that in the interior region is then given as

$\eta = K_m/\sum_{j=0}^{m} K_j$.

This article will also examine the relative energy distribution between different layers, and

to do this the method of Fuller and Fahy [28] is used. This requires the sound power in each

layer to be calculated first. However, the role of the PML in the outer region is to artificially

damp down outgoing waves and so the energy calculated in this region is physically

meaningless. Therefore, power flow is computed only in the inner fluid and those outer

[elastic] layers present, and so for an elastic layer the power flow is given as

$$W_j = -\pi \int_{\Omega_j} \text{Re}[\sigma_{zr} \cdot u_r^* + \sigma_{z\theta} \cdot u_\theta^* + \sigma_{zz} \cdot u_z^*] r dr \qquad j = 1 \text{ to } m - 1. \qquad (28)$$

For the inner fluid region, the sound power is given as

$$W_0 = \pi \omega^3 \int_{\Omega_0} \rho_0 \text{Re}[i\zeta^* \widetilde{\mathbf{p}}_0^* \cdot \widetilde{\mathbf{p}}_0] r dr. \qquad (29)$$

The energy ratio is then defined as the sum of the power in region Ω_0, divided by the sum

of the power in structure $W_S = \sum_{j=1}^{m-1} W_j$, so that

$$E_R = \frac{W_0}{W_S} = -\frac{\omega^3 \int_{\Omega_0} \rho_0 \text{Re}[i\zeta^* \widetilde{\mathbf{p}}_0^* \cdot \widetilde{\mathbf{p}}_0] r dr}{\sum_{j=1}^{m-1} \left[\int_{\Omega_j} \text{Re}[\sigma_{zr} \cdot u_r^* + \sigma_{z\theta} \cdot u_\theta^* + \sigma_{zz} \cdot u_z^*] r dr \right]}. \qquad (30)$$

3. Comparison between SAFE-PML and SBFEM

In this section, the SAFE-PML model is compared against SBFEM for a titanium elastic

rod immersed in motor oil [25]. The SAFE-PML solution is obtained using the method

presented in section 2.4, following the removal of the inner fluid section and setting the inner

radius $a_0 = 0$. Two different finite element discretisations are used for the SAFE-PML

approach: standard quadratic elements [16] and Gauss-Lobatto-Legendre spectral elements

[18, 29], with a Gauss quadrature scheme used for both types of element. For the PML, the

following co-ordinate stretching function is used [16]

$$\xi(r) = e^{\alpha \bar{r}} - i[e^{\beta \bar{r}} - 1], \qquad (31)$$

where $\bar{r} = (r - a_{m-1})/h$, and the thickness of the PML layer is $h = a_m - a_{m-1}$, with α

and β real valued constants. This stretching function was found by Duan et al. [16] to work

well for values of $\alpha = 4$ and $\beta = 5$ for quadratic elements. For the spectral element method,

a range of these parameters has been proposed [18], however in order to minimise the number

of variables to be investigated in the analysis that follows, and to avoid repetition of previous

investigations, values of $\alpha = 4$ and $\beta = 5$ are used for quadratic elements in sections 3 and 4,

14

and $\alpha = 5$ and $\beta = 6$ for spectral elements. Furthermore, the PML is attached directly to the outside of the pipe wall in order to minimise the size of the mesh required [16].

The SAFE-PML method is compared against the SBFEM results published by Gravenkamp et al. [25] for a titanium rod of radius of $a_1 = 1$ mm, a shear modulus $\mu_1 = 46.53$ GPa, a density $\rho_1 = 4.46$ g/cm^3 and a Possion's ratio of $v = 0.302$. For the surrounding motor oil: $c_m = 1.74$ km/s and $\rho_m = 0.87$ g/cm^3. First, convergence is examined for the PML by comparing results obtained for standard quadratic finite elements in Table 1, and spectral elements in Table 2, for the first two longitudinal modes at a frequency of 1.5 MHz.

Table 1. Convergence of wavenumbers γ for quadratic finite elements at 1.5 MHz for varying PML thickness and with fixed number of nodes in the rod.			
h	N_m	L(0,1)	L(0,2)
$0.2a_1$	7	0.76720 - 0.03992i	0.46818 - 0.43969i
$0.4a_1$	13	0.76745 - 0.03882i	0.46682 - 0.43961i
$0.6a_1$	19	0.76750 - 0.03892i	0.46697 - 0.43953i
$0.8a_1$	25	0.76749 - 0.03892i	0.46696 - 0.43955i
a_1	31	0.76749 - 0.03892i	0.46696 - 0.43955i

Table 2. Convergence of wavenumbers γ for spectral finite elements at 1.5 MHz for varying PML thickness and with fixed number of nodes in the rod.			
h	N_m	L(0,1)	L(0,2)
$0.2a_1$	7	0.76515 - 0.03956i	0.46796 - 0.44219i
$0.4a_1$	13	0.76733 - 0.03893i	0.46693 - 0.43976i
$0.6a_1$	19	0.76749 - 0.03892i	0.46694 - 0.43953i
$0.8a_1$	25	0.76749 - 0.03892i	0.46695 - 0.43952i
a_1	31	0.76750 - 0.03892i	0.46696 - 0.43951i

In Tables 1 and 2, the SAFE-PML method is seen to converge quickly for what is a relatively straightforward problem. In these tables N_m is the number of nodes in the PML, and in Table 1 ten quadratic elements are fixed for the rod, so that $N_r = 21$. This is

equivalent to 43 nodes per wavelength for the bulk shear wave at 1.5MHz, which delivers an element density that is higher than the usual requirement in a finite element model; however, the number of elements is chosen to remove the influence of element density in the rod region, so that the focus is entirely on the PML region [as this is where the model differs from the SBFEM approach]. The element density in the PML region is 35 nodes per wavelength and this is kept constant in Table 1. For spectral elements, one element of order 20 is used for the rod, and one spectral element is used in the PML with an order equal to $(N_m - 1)$. This gives identical degrees of freedom for the quadratic and spectral elements so that a meaningful comparison for accuracy can be made for the same solution time.

It can be seen in Tables 1 and 2 that for a PML thickness of $h = 0.2a_1$ both models converge to two decimal places for the non-dimensional wavenumber γ using only seven nodes in the PML region. As the PML thickness is increased, the eigenvalues converge to four decimal places, so that the quadratic and spectral elements give almost identical values when $h = a_1$. Further, for $h = 0.4a_1$ the computation time for quadratic and spectral elements is 6.5 ms and 6.1 ms per frequency, respectively. The analysis in Tables 1 and 2 examines a change in the size of the PML, however it is possible that in this analysis the errors introduced by the PML are greater than the discretisation errors associated with the quadratic and spectral elements. Accordingly, in Tables 3 and 4 the convergence of the quadratic and spectral elements is examined with the width of the PML fixed at $h = a_1$. It can be seen in Tables 3 and 4 that the rate of convergence when the PML width is fixed is similar to that seen in Tables 1 and 2. Accordingly, no discernible difference in the rate of convergence is seen between the two types of finite element discretisation used for the PML.

Table 3. Convergence of wavenumbers γ for quadratic finite elements at 1.5 MHz for fixed PML thickness and with fixed number of nodes in the rod.			
h	N_m	L(0,1)	L(0,2)
a_1	5	0.79690 - 0.07193i	0.49217 - 0.39481i
a_1	9	0.76849 - 0.03548i	0.46337 - 0.44024i
a_1	17	0.76763 - 0.03895i	0.46706 - 0.43928i
a_1	33	0.76749 - 0.03892i	0.46696 - 0.43955i
a_1	65	0.76750 - 0.03892i	0.46696 - 0.43954i

Table 4. Convergence of wavenumbers γ for spectral finite elements at 1.5 MHz for fixed PML thickness and with fixed number of nodes in the rod.			
h	N_m	L(0,1)	L(0,2)
a_1	5	0.79559 - 0.03371i	0.45174 - 0.41437i
a_1	9	0.77185 - 0.03599i	0.46273 - 0.43464i
a_1	17	0.76754 - 0.03902i	0.46714 - 0.43951i
a_1	33	0.76750 - 0.03892i	0.46695 - 0.43952i
a_1	65	0.76751- 0.03891i	0.46698 - 0.43957i

The results reported in Tables 1-4 are designed to illustrate rates of convergence for the PML. In Tables 5 and 6, rates of convergence for the rod are also investigated, this time with a fixed value of $N_m = 33$ in the PML.

Table 5. Convergence of wavenumbers γ for quadratic finite elements at 1.5 MHz for fixed PML thickness and with fixed number of nodes in the PML.			
h	N_r	L(0,1)	L(0,2)
a_1	5	0.76426 - 0.03824i	0.47025 - 0.45536i
a_1	9	0.76729 - 0.03888i	0.46714 - 0.44059i
a_1	17	0.76749 - 0.03892i	0.46697 - 0.43959i
a_1	33	0.76750 - 0.03892i	0.46696 - 0.43952i

Table 6. Convergence of wavenumbers γ for spectral finite elements at 1.5 MHz for fixed PML thickness and with fixed number of nodes in the PML.			
h	N_r	L(0,1)	L(0,2)
a_1	5	0.76786 - 0.03890i	0.46682 - 0.43570i
a_1	9	0.76749 - 0.03892i	0.46695 - 0.43951i
a_1	17	0.76748 - 0.03888i	0.46692 - 0.43951i
a_1	33	0.76749 - 0.03892i	0.46696 - 0.43952i

In Tables 5 and 6 good convergence is achieved for quadratic and spectral elements with $N_r = 17$, so that the choice of $N_r = 21$ in Tables 1-4 is shown to be adequate. It is evident in Tables 5 and 6 that the spectral element method converges more quickly and outperforms quadratic elements at the lowest values of N_r. This behaviour was also observed at other frequencies (not shown here). This improvement in performance is not seen for the PML discretisation, and this is thought to be because it is harder to achieve accurate predictions with low mesh densities inside the PML. This is because numerical errors associated with the coordinate stretching function and numerical damping in the PML are likely to be present at low mesh densities, and these serve to compromise the relative advantages normally observed with the spectral element method. Thus, the results presented in Tables 1-6 illustrate that some of the advantages normally associated with the spectral element method are not necessarily retained when studying a PML, at least for the eigenproblem examined in this article.

In Figs. 2 and 3, the dispersion curves for this example are shown using $N_r = 21$, $N_m = 13$ and $h = 0.4a_1$, after enforcing $\eta \leq 0.9$ to remove the radiation modes. Figures 2 and 3 show excellent agreement between the SAFE-PML model developed here and the SBFEM approach of Gravenkamp et al. [25] [note that additional torsional, or shear, modes for the rod have been added to these figures, labelled here T(0,1) and T(0,2)]. The dispersion curves use 300 data points and were obtained in 1.844 seconds. In the article by Gravenkamp et al. [25] it was noted that a spectral element of order six, with five iterations, delivered a converged solution in about 2 seconds for the entire frequency range. It is difficult to achieve an exact comparison between solution times, because the number of data points in the results present by Gravenkamp et al. [25] is unknown, as well as the solution accuracy and relative computer performance; however, the time taken using the SAFE-PML approach is at least of the same order as that of Gravenkamp et al. [25]. Furthermore, Kalkowski et al. [18] quote a solution

time of 9.1 ms for one frequency step and this gives a solution time of 2.7 seconds for 300 data points.
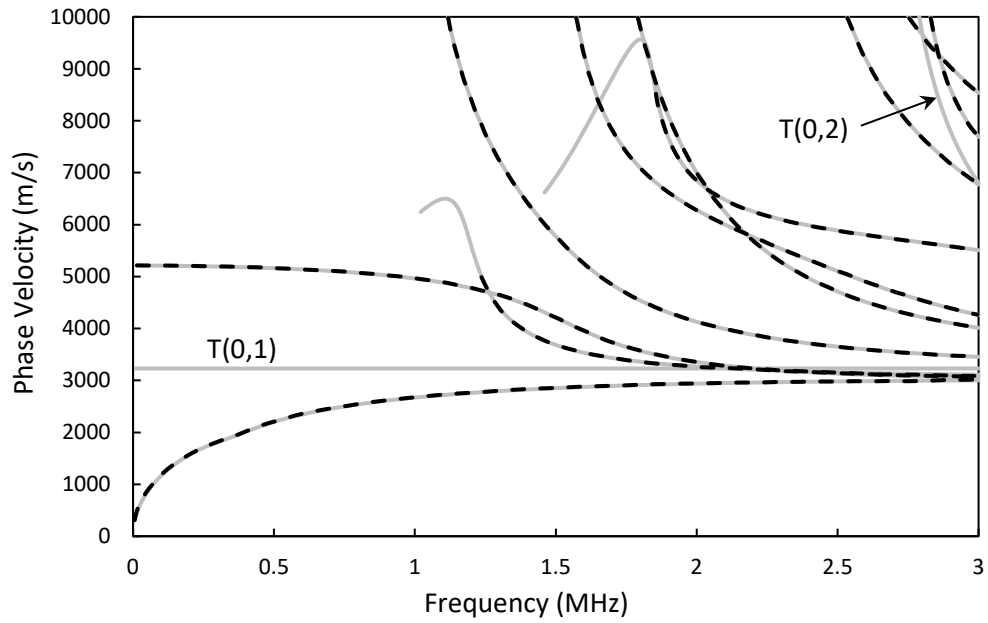

Figure 2. Phase velocity for titanium rod immersed in engine oil.
————, SAFE-PML solution;   − − − −, SBFEM solution [21].
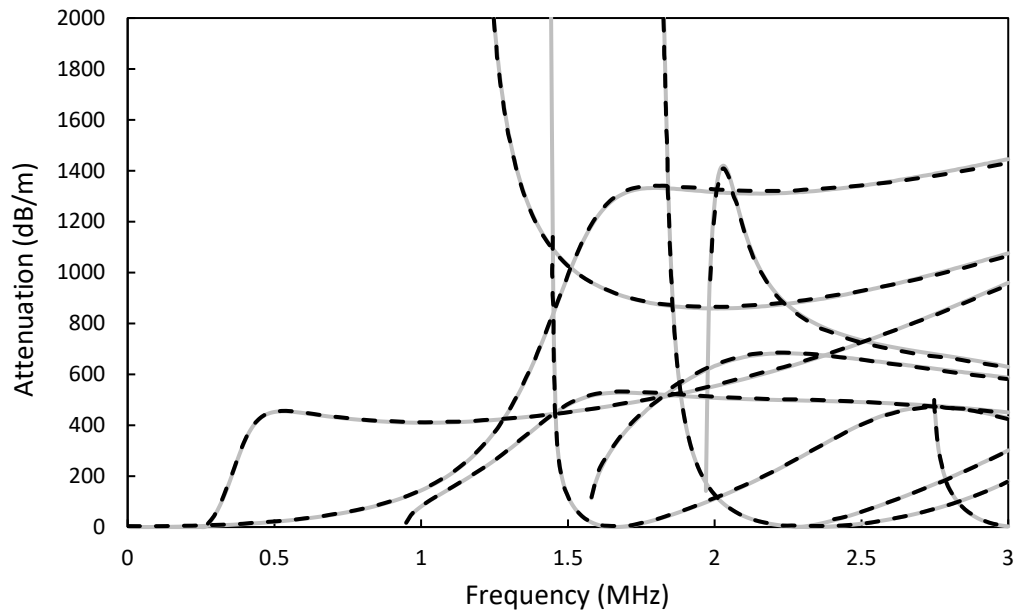

Figure 3. Attenuation for titanium rod immersed in engine oil.
————, SAFE-PML solution;   − − − −, SBFEM solution [21].

It is seen in Figs. 2 and 3 that all three approaches are capable of providing solutions in a very similar timescale and that the recent advances in the SAFE-PML approach have now delivered a method that is comparable, in terms of computational efficiency, to that of the SBFEM approach. Each method can of course be further speeded up if one further relaxes the requirement for accuracy, as if often the case when plotting dispersion curves. Thus, an optimised SAFE-PML approach is clearly worthy of consideration when attempting to study this type of problem. The question then shifts to whether these observations scale up for bigger and more complex problems such as buried pipelines. Accordingly, in the next two sections more complex problems are examined using the SAFE-PML method, and relative solution speeds are compared against those found in this section and potential challenges are identified.

4. SAFE-PML convergence for a fluid-filled immersed pipe

The SAFE-PML method is applied in this section to a fluid-filled immersed pipe, as this is relevant to many engineering applications. Fluid filled pipes typically generate a large number of eigenmodes over the frequency range of interest and this makes the identification and labelling of modes difficult, especially as many leaky modes transfer their energy from the wall to the fluid, and *vice versa* [28]. In this article, the modes are labelled as follows: $FS(n, m)$, $SF(n, m)$, $FL(n, m)$, and $T(0, m)$, where n stands for circumferential mode order, and m for the sequence of modes in each circumferential family. Each mode is labelled according to the relative energy distribution between the internal fluid (Ω_0) and the pipe substrate (Ω_1), and the decision on which labels to choose is based on behaviour at low frequencies and/or close to modal cut on (see later plots). This means that for an FS mode, the acoustic energy lies predominantly in the fluid at lower frequencies, whereas at higher frequencies energy transfers from the fluid into the structure. An SF mode starts out as

predominantly structural mode, with close equivalents to those found in a pipe *in vacuo*, and then transfers its energy from the structure into the fluid at higher frequencies. This notation also encourages the continued use of $T(0, m)$ for shear (torsional) modes, as they do not interact with the fluid. Finally, there are additional modes whose energy remains predominantly in the fluid over a wide frequency range, and these modes appear only when the fluid-filled pipe is further immersed in a fluid or buried in a solid; these modes are labelled here $FL(n, m)$. Note also that at higher frequencies progressive numbers of SF modes begin to cut-on, and at frequencies very close to cut-on these modes do not propagate, so that their energy oscillates locally and lies mostly within the fluid; however, as the mode moves away from its cut-on frequency, energy rapidly transfers from the fluid to the structure and it takes on the characteristics of a structural mode. Accordingly, the limiting behaviour seen at cut-on has little practical relevance and so these modes are also considered to be $SF(n, m)$ modes.

The water-filled cast-iron pipe studied by Long et al. [30] is analysed in this section. The dimensions of the pipe are $a_0 = 0.127$ m, and $a_1 = 0.143$ m, with the pipe wall thickness $t_w = a_1 - a_0$; for cast-iron, $c_{T_1} = 2500$ m/s, $c_{L_1} = 4500$ m/s, and $\rho_1 = 7100$ kg/m^3; for water, $c_0 = 1480$ m/s, and $\rho_0 = 1000$ kg/m^3. Tables 7 and 8 examine the convergence of wavenumbers γ for this pipe using quadratic and spectral elements at a frequency of 5 kHz.

Table 7. Convergence of wavenumbers γ for quadratic finite elements at 5 kHz				
h	N_m	SF(0,1)	FS(0,1)	FL(0,1)
t_w	9	0.57674 - 0.03988i	3.03408 + 0.00033i	1.50975 - 0.53181i
$2t_w$	17	0.57683 - 0.03993i	3.03348 + 0.00016i	1.52561 - 0.55257i
$3t_w$	25	0.57683 - 0.03993i	3.03344 + 0.00001i	1.52987 - 0.55370i
$4t_w$	33	0.57683 - 0.03993i	3.03345 + 0.00000i	1.53034 - 0.55329i
$5t_w$	41	0.57683 - 0.03993i	3.03345 + 0.00000i	1.53033 - 0.55321i

Table 8. Convergence of wavenumbers γ for spectral finite elements at 5 kHz				
h	N_m	SF(0,1)	FS(0,1)	FL(0,1)
t_w	9	0.57696 - 0.04009i	3.02513 + 0.00211i	1.59134 - 0.74657i
$2t_w$	17	0.57683 - 0.03993i	3.03378 - 0.00013i	1.53657 - 0.56095i
$3t_w$	25	0.57683 - 0.03993i	3.03347 + 0.00001i	1.53051 - 0.55411i
$4t_w$	33	0.57683 - 0.03993i	3.03348 - 0.00000i	1.53030- 0.55330i
$5t_w$	41	0.57683 - 0.03993i	3.03348 + 0.00000i	1.53031 - 0.55322i

For the quadratic elements, 32 are used in the internal fluid region and 4 in the pipe region. For the spectral elements, one element of order 64 is used in the internal fluid region, and one of order 8 is used in the pipe region. This delivers an equivalent degrees of freedom between the quadratic and spectral finite element models so that they can be compared. The rate of convergence for a number of modes is compared in Tables 7 and 8, for different PML thicknesses. It can be seen that when a steady increase in the PML thickness is accompanied by an increase in the number of degrees of freedom, convergence to four decimal places can quickly be achieved for this more complex problem. Furthermore, the quadratic and spectral elements continue to provide similar results when examining convergence for the PML.

This problem presents an increase in complexity when compared to the immersed rod in the previous section. This is because the stress distributions in a pipe wall are more complex than for a rod, and new modes also appear. Furthermore, this problem has been deliberately chosen to illustrate the challenges presented by trapped modes. For the material parameters and frequency range chosen, the fluid inside the pipe generates the trapped mode FS(0,1). This mode is characterised by a displacement field that decays exponentially in the outer fluid/solid region [13]. In Tables 7 and 8, convergence for this mode is seen to be slightly slower than for the other modes (note that the imaginary part should, by definition, be zero). Slower convergence arises for trapped modes because the PML parameters are designed primarily to absorb leaky modes. This is achieved using a complex stretching function that

absorbs energy over the thickness of the PML. However, trapped modes decay exponentially away from the pipe wall, which means there is a very rapid variation in the modal eigenfunction over a very short distance close to the pipe wall. This means that a PML with a mesh distribution that is designed to absorb leaky modes over the entire width of the PML will not be optimal for capturing the behaviour of a trapped mode because there will be insufficient elements very close to the pipe wall. Furthermore, it is necessary also to enforce zero displacement for the trapped modes in the outer region, and convergence for this boundary condition is achieved by progressively increasing the thickness of the PML. Thus, trapped modes incur additional computational expenditure as the mesh must address two opposing criteria.

Accordingly, a relatively thick PML, with $h = 4t_{\mathrm{w}}$, is used in this problem to find the trapped and leaky modes, with a proportionally higher mesh density when compared to the rod studied in the previous section. Tables 7 and 8 indicate good converge with one spectral element of order 64, 8 and 32 for the inner fluid, pipe wall and PML, respectively. The increase in mesh density means that it takes 5.9 seconds to generate dispersions curves for 300 frequency steps, and the dispersion curves are shown in Fig. 4. The SAFE-PML method is also compared against the analytic global matrix solution DISPERSE [30] in Fig. 4, and one can see that the SAFE-PML method works successfully down to low frequencies and accurately captures trapped as well as leaky modes.
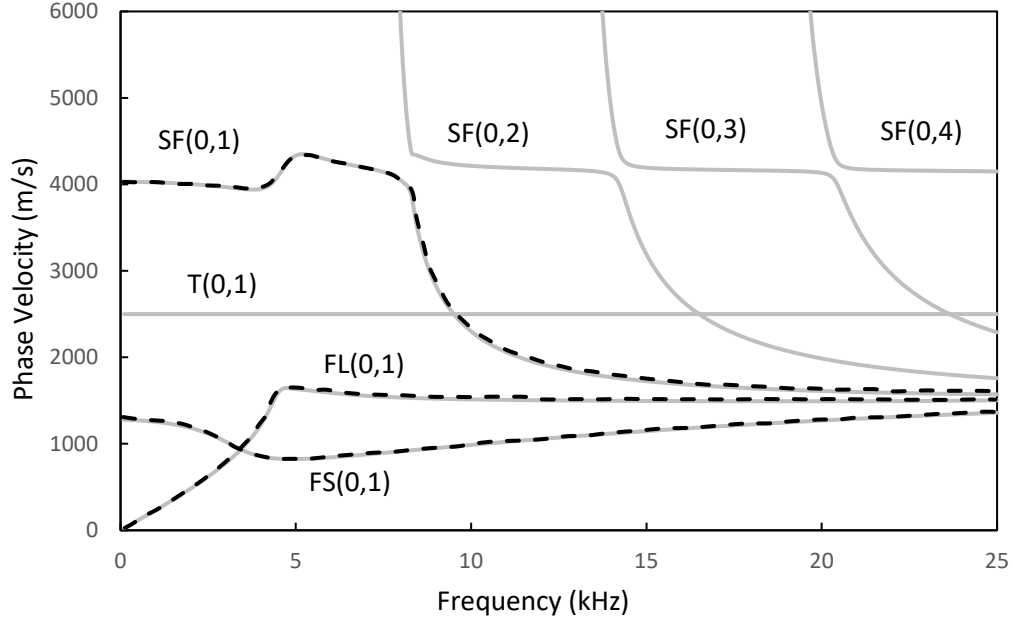
Figure 4. Phase velocity in a water-filled cast iron pipe immersed in water. ———, SAFE-PML solution; – – – – –, analytic solution (DISPERSE) [30].

It is interesting also to investigate the relative energy distribution in the pipe, as the energy transport characteristics of particular modes are important in determining the likely speed and accuracy of a particular numerical approach. The distribution of energy in fluid-filled pipes has been studied before, see for example Fuller and Fahy [28], however this is less well explored for the more complex problem of buried or immersed pipes. Accordingly, relative energy distribution is explored here using the ratio, E_R, defined in Eq. (30); remembering that this is the ratio of the sound power contained within the internal fluid region to that in the pipe wall, so that values of E_R greater than unity mean that the energy resides predominantly in the internal fluid, and *vice versa*. The relative energy distribution for the immersed cast-iron water-filled pipe is examined in Fig. 5, and the modal attenuation is also reported in Fig. 6, as this helps to explain the changes in behaviour caused by the surrounding fluid.
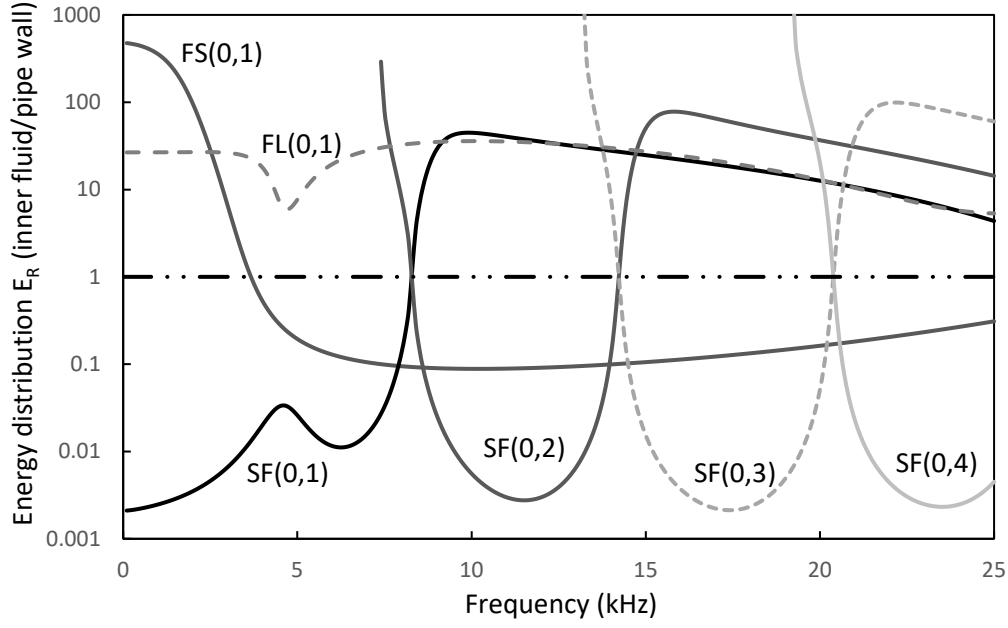
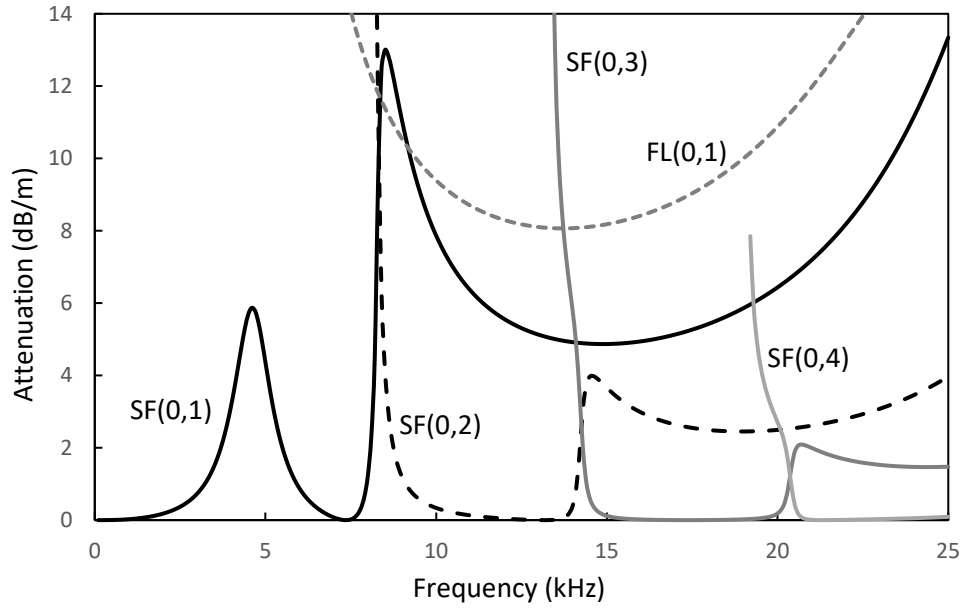Fig. 5. Energy distribution in a water-filled cast iron pipe immersed in water.

Fig. 6. Modal attenuation in a water-filled cast iron pipe immersed in water.

A comparison between the energy distribution and modal attenuation in Figs. 5 and 6

shows that the attenuation of SF(0,1) peaks at about 5 kHz and then reduces as energy no

longer transfers out of the structure above this frequency. However, the energy in this mode

is then seen to transfer into the fluid above 8kHz, which causes a rapid increase in attenuation

as the mode begins to radiate energy outwards. That is, if a mode has high levels of attenuation in a lossless system then this must be caused by energy leakage/radiation into the outer fluid. This type of behaviour can also be seen for the fluid mode FL(0,1), with the energy in the mode continuing to reside in the fluid over the entire frequency range in Fig 5; however, in Fig. 6 the modal attenuation reveals that as the frequency is increased up to around 14 kHz the attenuation drops. This indicates that energy is transferring from the outer to the inner fluid. Furthermore, the high levels of attenuation indicate that the FL(0,1) mode is a radiation type mode at low frequencies. In contrast, the higher order SF modes have frequency bands where the energy resides mainly in the pipe wall, and so the attenuation of these modes is generally much lower, at least up until the next higher order SF mode cuts-on. It is possible, therefore, that the SF modes, and especially the higher order SF modes, may be useful in non-destructive testing. However, Figs. 5 and 6 do serve to illustrate the complexity of the problem once one moves on to study pipelines, and the energy transfer between the fluid and the structure makes the generation of fast numerical algorithms challenging.

5. Convergence of the SAFE-PML method for a fluid-filled buried pipe

In this section, the surrounding medium is changed from a fluid to a solid, as this generates a different modal structure. The 8 inch schedule 40 pipe studied by Duan et al. [16] is analysed here, so that $a_0 = 101.36$ mm and $a_1 = 109.54$ mm. The pipe is filled with water (see properties in the previous section) and made of steel, with $c_{T_1} = 3260$ m/s, $c_{L_1} = 5960$ m/s, and $\rho_1 = 7932$ kg/m^3. The pipe is also buried in soil, with $c_{T_m} = 300$ m/s, $c_{L_m} = 1540$ m/s, and $\rho_m = 2000$ kg/m^3 [16]. Note that values of $\alpha = 5$ and $\beta = 6$ are used for both quadratic and spectral elements in this section. Tables 9 and 10 examine the convergence of wavenumbers for this pipe using quadratic and spectral elements at a frequency of 16 kHz.

Table 9. Convergence of wavenumbers γ for quadratic finite elements at 16 kHz				
h	N_m	SF(0,1)	FS(0,1)	FL(0,2)
$0.2t_w$	7	0.59393 - 0.02821i	3.19834 - 0.02782i	2.17909 - 0.01171i
$0.6t_w$	17	0.59456 - 0.02850i	3.20827 - 0.03797i	2.17263 - 0.00974i
t_w	27	0.59458 - 0.02850i	3.20988 - 0.03738i	2.17189 - 0.00978i
$2t_w$	53	0.59458 - 0.02850i	3.20974 - 0.03739i	2.17180 - 0.00983i
$3t_w$	79	0.59458 - 0.02850i	3.20974 - 0.03739i	2.17180 - 0.00983i

Table 10. Convergence of wavenumbers γ for spectral finite elements at 16 kHz				
h	N_m	SF(0,1)	FS(0,1)	FL(0,2)
$0.2t_w$	7	0.59361 - 0.02852i	3.19640 - 0.04910i	2.17976 - 0.01238i
$0.6t_w$	17	0.59458 - 0.02849i	3.20943 - 0.03740i	2.17256 - 0.00965i
t_w	27	0.59458 - 0.02850i	3.20980 - 0.03740i	2.17187 - 0.00978i
$2t_w$	53	0.59458 - 0.02850i	3.20979 - 0.03740i	2.17180 - 0.00983i
$3t_w$	79	0.59458 - 0.02850i	3.20979 - 0.03740i	2.17180 - 0.00983i

For the quadratic elements, 30 are used in the internal fluid region and 4 in the pipe. For the spectral elements, one element of order 60 is used in the internal fluid region, and one element of order 8 for the pipe; this delivers an equivalent number of degrees of freedom for the quadratic and spectral elements. The element density in the PML region is also kept at 24 nodes per wavelength for both approaches. The convergence of three modes is examined in Tables 9 and 10, and here it can be seen that a steady increase of PML thickness delivers convergence to four decimal places. Furthermore, the quadratic and spectral elements are again seen to deliver similar results when studying convergence of the PML. Note that for the other modes propagating at this frequency the convergence is much better and so these modes are not included in Tables 9 and 10.

To plot the dispersion curves for this example, a PML of thickness $h = 2t_w$ is chosen with $N_m = 53$. This requires 47.74 seconds to generate dispersion curves with 300 frequency steps. This represents a significant increase in solution time when compared to the immersed

pipe/rod, and this is because the number of degrees of freedom in the elastic PML region is $(3 \times N_m)$ larger than that in the acoustic PML region (N_m). Moreover, the surrounding soil now supports both compressional and shear waves and accurately capturing all the leaky modes is more challenging when compared to a fluid region. This change in complexity is best illustrated in the phase velocity diagram shown in Fig. 7, along with the energy distribution in Fig. 8 and the attenuation in Fig. 9.
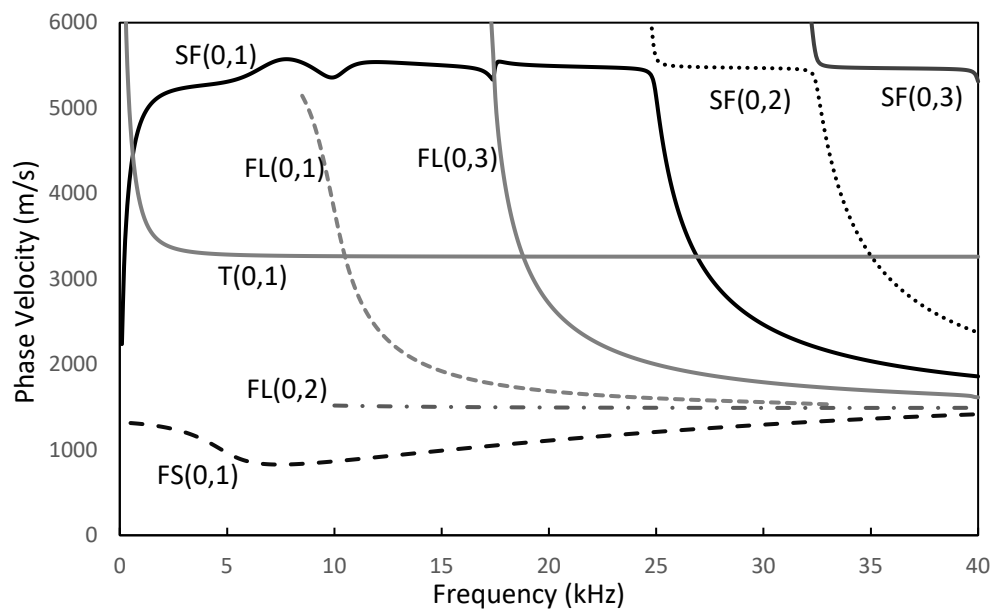

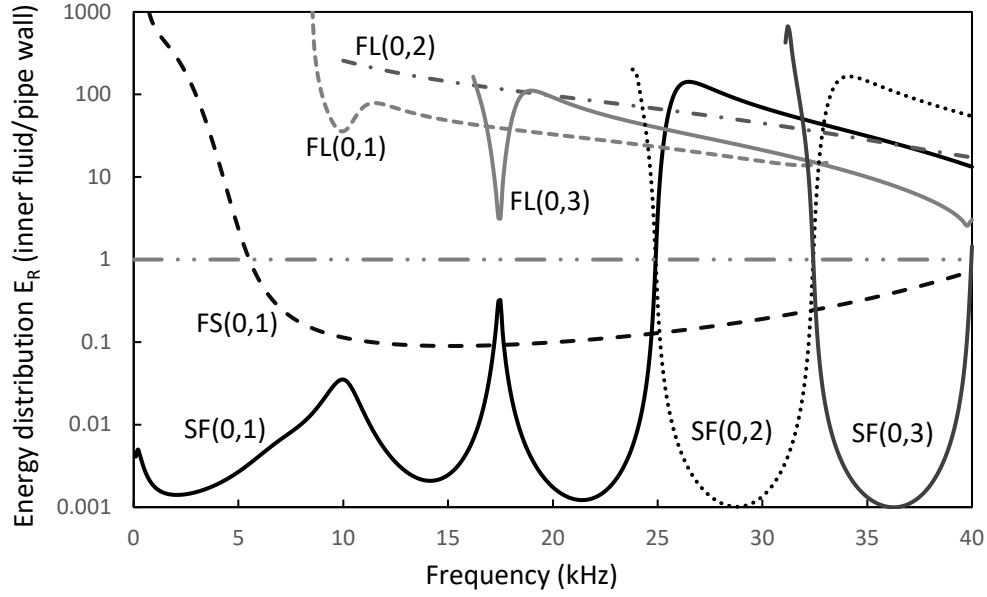Figure 7. Phase velocity in a water-filled steel pipe buried in soil.

Figure 8. Energy distribution in a water-filled steel pipe buried in soil.
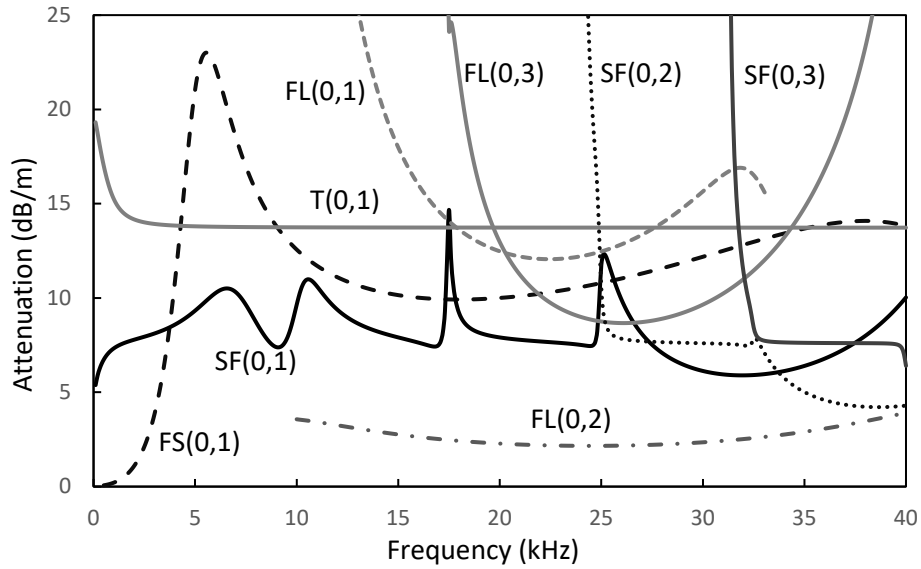

Figure 9. Modal attenuation in a water-filled steel pipe buried in soil.

Figures 7 - 9 display very different behaviour when compared to the immersed pipe in the previous section. This illustrates that one cannot expect simply to extrapolate, or scale, computational efficiency from one scenario to another for any given model. Clearly, the addition of a solid outer structure has required the addition of a thicker PML, with many more degrees of freedom required to deliver an accurate solution over a wide frequency

range. However, the solution time presented here for the SAFE-PML is still considered to be reasonable given the complexity of the problem, and it is shown that it is possible to generate dispersion curves over a wide frequency range in about 1 minute using relatively modest computational hardware.

Figures 7 - 9 also illustrate another difficulty associated with plotting dispersion curves for buried and immersed structures. In both figures, the FL(0,2) mode is plotted only at frequencies higher than about 10 kHz. At 10 kHz the mode is deemed to transition from a radiation to a leaky mode. The kinetic energy ratio $\eta = 0.9$ is used to define this transition point, so that for $\eta < 0.9$ this mode is added to Figs. $7 - 9$, hence the abrupt appearance of FL(0,2). The choice of $\eta = 0.9$ is of course arbitrary and this will affect the extent to which FL(0,2) appears in Figs. 7 - 9. Moreover, the value of η also changes with the thickness of the PML and this means that it is often difficult to compare dispersion curves generated by different authors for the same problem. For example, Kalkowski et al. [18] compare their dispersion curves against those of Nguyen et al. [14] and Duan et al. [16]. In Fig. 3 of their paper Kalkowski et al. terminate their dispersion curves at frequencies higher than those used by Duan et al, and so discrepancies between the two results seem to be present. However, these differences are caused only by the different choice of η, the PML thickness/mesh density, and/or the maximum magnitude of the imaginary part of the wavenumber; that is, the numerical results for all studies agree with one another.

6. Addition of material damping in the outer layer

The predictions presented so far assume that the medium surrounding the pipe is perfect and elastic. It is, however, well known that materials such as soil have internal damping present within their structure and that this may affect the propagation of an elastic wave. Damping will affect the attenuation of a particular eigenmode and the effect of the material damping may dominate over the attenuation caused by the energy radiating away from a

structure [30, 31]. The influence of this material damping can readily be accommodated in the SAFE-PML model simply by adding complex material properties to the mass and stiffness matrices in the outer region. This is straightforward because these mass and stiffness matrices are already complex to accommodate the PML, and so no further alterations to the model are required.

For example, the shear and longitudinal bulk wave velocities in the soil may be written as $c_{T_m} = 1/[1/\tilde{c}_T - i\tilde{\alpha}_T]$ and $c_{L_m} = 1/[1/\tilde{c}_L - i\tilde{\alpha}_L]$, respectively [16]. The appropriate choice of $\tilde{\alpha}_{T,L}$ then enables the material damping to be accounted for. Values of $\tilde{c}_T = 300$ m/s, $\tilde{c}_L = 1540$ m/s, $\tilde{\alpha}_T = 0.5 \times 10^{-3}$ s/m, and $\tilde{\alpha}_L = 0.1 \times 10^{-3}$ s/m are reported for soil by Duan et al. [16]. These values may then be added to the SAFE-PML model and dispersion curves obtained in the usual way. Example dispersion curves for modal attenuation are shown in Fig. 10, for the pipe geometry studied in the previous section and with $h = 2t_w$ and $N_m = 53$.
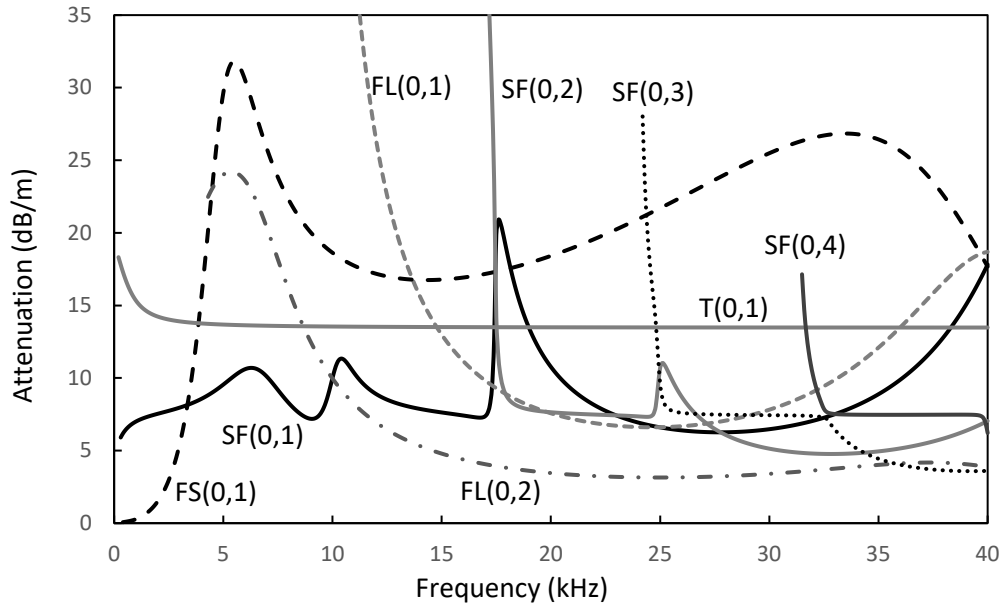

Figure 10. Modal attenuation in the water-filled steel pipe buried in damping soil.

It can be seen that when material damping is present the attenuation of a number of modes changes significantly, although it is interesting to note that this does not always deliver an increase in attenuation. A complex pattern of behaviour is observed where the damping may change the balance of energy between the fluid and the soil and in turn this effects the way in which energy transfers between the different regions. A more detailed analysis awaits further investigation, however it is shown here that material damping may readily be included into a SAFE-PML model.

7. Conclusions

This article uses a weighted residual approach to deliver a one-dimensional SAFE-PML model that is aimed at obtaining the coupled eigenmodes for fluid-filled immersed and buried pipes. The speed and accuracy of the method is examined by comparing predicted dispersion curves against those obtained using the SBFEM method, and it is demonstrated that an optimised one dimensional SAFE-PML approach is capable of delivering fast and efficient eigensolutions for pipes and rods. Moreover, solution times using the SAFE-PML approach are almost identical to those found using the SBFEM for an immersed rod [25]. The SAFE-PML approach is then applied to fluid-filled buried and immersed pipes, and for a fluid-filled 8 inch schedule 40 pipe buried in soil the solution time for a single frequency is about 160 ms, once the eigenmodes have been computed and sorted on relatively modest computer hardware. Accordingly, it is demonstrated that the SAFE-PML method is capable of delivering fast and accurate solutions that are comparable to those found using other methods, whilst retaining the flexibility to accommodate more complex pipe applications, including material damping in the outer layer.

The relative accuracy and efficiency of quadratic and higher order spectral finite elements is also examined for the PML. To enable a consistent comparison, the number of degrees of freedom in each region is kept constant and convergence is examined for different PML

thicknesses. This reveals no practical difference in the relative rates of convergence for the two methods when changing the density of the mesh in the PML. Accordingly, it is concluded that the benefits normally associated with the use of spectral elements are not necessarily present when discretising a PML for use in an eigensolution such as the one studied here.

The SAFE-PML approach enables the straightforward calculation of the relative distribution of energy between the inner fluid and the pipe wall once the dispersion problem has been solved. This is shown to provide an important insight into the behaviour of individual eigenmodes, and when coupled with plots of modal attenuation and mode shape this illustrates why a careful choice of PML is necessary when identifying and tracking relevant modes. This is particularly important when computing trapped modes, where a relatively thick PML, coupled to a fine mesh density close to the pipe, is required. Furthermore, the arbitrary choice of the kinetic energy ratio η means that problems are seen to arise when determining the frequency at which a mode is said to "transition" from a radiating to leaky mode. This is an issue that cannot be avoided when using an artificial absorbing layer to damp down outward propagating waves in an eigensolution. However, this problem tends to be most obvious when studying higher order modes, and for most practical problems this is not thought to present a limitation of the method. Accordingly, it is concluded that the SAFE-PML approach is capable of providing fast and accurate solutions for fluid-filled buried and immersed pipelines, and for the problems studied here this approach is at least equivalent to the speed and accuracy found using the SBFEM approach.

Appendix A

For elastic layers Ω_j (with j extending from 1 to $m-1$ if the outer layer Ω_m is a fluid, and

from 1 to m if it is an elastic solid):

$$\mathbf{R}_{10} = \mathbf{K}_1 - 2\mathbf{K}_2 + \mathbf{K}_3 + (n^2 + 2)\mathbf{M}_2 - \mathbf{M}_7, \text{ and } \mathbf{R}_{12} = \mathbf{M}_1 \qquad \text{(A1a, b)}$$

$$\boldsymbol{\Theta}_{20} = -\mathbf{K}_6 + 2\mathbf{K}_2 + \mathbf{K}_2^\mathrm{T} - n^2\mathbf{M}_3 - 2\mathbf{M}_2 + \mathbf{M}_7, \text{ and } \boldsymbol{\Theta}_{22} = -\mathbf{M}_1 \qquad \text{(A2a, b)}$$

$$\mathbf{Z}_{30} = \mathbf{K}_6 - \mathbf{K}_2 + n^2\mathbf{M}_2 - \mathbf{M}_7, \text{ and } \mathbf{Z}_{32} = \mathbf{M}_6 \qquad \text{(A3a, b)}$$

$$\boldsymbol{\Theta}_{10} = n[\mathbf{K}_2 - \mathbf{K}_3 - 3\mathbf{M}_2], \text{ and } \mathbf{Z}_{11} = [\mathbf{K}_4 - \mathbf{K}_5] \qquad \text{(A4a, b)}$$

$$\mathbf{R}_{20} = n[\mathbf{K}_3^\mathrm{T} - \mathbf{K}_2^\mathrm{T} + \mathbf{M}_4], \text{ and } \mathbf{Z}_{21} = -n\mathbf{M}_5 \qquad \text{(A5a, b)}$$

$$\mathbf{R}_{31} = [\mathbf{K}_5^\mathrm{T} - \mathbf{K}_4^\mathrm{T} + \mathbf{M}_5], \text{ and } \boldsymbol{\Theta}_{31} = -n\mathbf{M}_5 \qquad \text{(A6a, b)}$$

The matrices that make up these equations are given below. In the matrices that follow,

the PML is assumed to be elastic, so that these equations apply to a buried pipe. However, if

the pipe is immersed, then the integrals over Ω_m should be removed from these matrices.

$$\mathbf{K}_1 = \sum_{j=1}^{m-1} (\lambda_j + 2\mu_j) \int_{\Omega_j} \frac{\partial \mathbf{W}^\mathrm{T}}{\partial r} \frac{\partial \mathbf{N}}{\partial r} dr + (\lambda_m + 2\mu_m) \int_{\Omega_m} \frac{1}{\xi} \frac{\partial \mathbf{W}^\mathrm{T}}{\partial r} \frac{\partial \mathbf{N}}{\partial r} dr \qquad \text{(A7)}$$

$$\mathbf{K}_2 = \sum_{j=1}^{m-1} \mu_j \int_{\Omega_j} \frac{1}{r} \mathbf{W}^\mathrm{T} \frac{\partial \mathbf{N}}{\partial r} dr + \mu_m \int_{\Omega_m} \frac{1}{\tilde{r}} \mathbf{W}^\mathrm{T} \frac{\partial \mathbf{N}}{\partial r} dr \qquad \text{(A8)}$$

$$\mathbf{K}_3 = \sum_{j=1}^{m-1} \lambda_j \int_{\Omega_j} \frac{1}{r} \frac{\partial \mathbf{W}^\mathrm{T}}{\partial r} \mathbf{N} dr + \lambda_m \int_{\Omega_m} \frac{1}{\tilde{r}} \frac{\partial \mathbf{W}^\mathrm{T}}{\partial r} \mathbf{N} dr \qquad \text{(A9)}$$

$$\mathbf{K}_4 = \sum_{j=1}^{m-1} \mu_j \int_{\Omega_j} \mathbf{W}^\mathrm{T} \frac{\partial \mathbf{N}}{\partial r} dr + \mu_m \int_{\Omega_m} \mathbf{W}^\mathrm{T} \frac{\partial \mathbf{N}}{\partial r} dr \qquad \text{(A10)}$$

$$\mathbf{K}_5 = \sum_{j=1}^{m-1} \lambda_j \int_{\Omega_j} \frac{\partial \mathbf{W}^\mathrm{T}}{\partial r} \mathbf{N} dr + \lambda_m \int_{\Omega_m} \frac{\partial \mathbf{W}^\mathrm{T}}{\partial r} \mathbf{N} dr \qquad \text{(A11)}$$

$$\mathbf{K}_6 = \sum_{j=1}^{m-1} \mu_j \int_{\Omega_j} \frac{\partial \mathbf{W}^\mathrm{T}}{\partial r} \frac{\partial \mathbf{N}}{\partial r} dr + \mu_m \int_{\Omega_m} \frac{1}{\xi} \frac{\partial \mathbf{W}^\mathrm{T}}{\partial r} \frac{\partial \mathbf{N}}{\partial r} dr \qquad \text{(A12)}$$

$$\mathbf{M}_1 = \sum_{j=1}^{m-1} \mu_j \int_{\Omega_j} \mathbf{W}^\mathrm{T}\mathbf{N}dr + \mu_m \int_{\Omega_m} \xi\mathbf{W}^\mathrm{T}\mathbf{N}dr \tag{A13}$$

$$\mathbf{M}_2 = \sum_{j=1}^{m-1} \mu_j \int_{\Omega_j} \frac{1}{r^2}\mathbf{W}^\mathrm{T}\mathbf{N}dr + \mu_m \int_{\Omega_m} \frac{\xi}{\tilde{r}^2}\mathbf{W}^\mathrm{T}\mathbf{N}dr \tag{A14}$$

$$\mathbf{M}_3 = \sum_{j=1}^{m-1} (\lambda_j + 2\mu_j) \int_{\Omega_j} \frac{1}{r^2}\mathbf{W}^\mathrm{T}\mathbf{N}dr + (\lambda_m + 2\mu_m) \int_{\Omega_m} \frac{\xi}{\tilde{r}^2}\mathbf{W}^\mathrm{T}\mathbf{N}dr \tag{A15}$$

$$\mathbf{M}_4 = \sum_{j=1}^{m-1} (\lambda_j + 4\mu_j) \int_{\Omega_j} \frac{1}{r^2}\mathbf{W}^\mathrm{T}\mathbf{N}dr + (\lambda_m + 4\mu_m) \int_{\Omega_m} \frac{\xi}{\tilde{r}^2}\mathbf{W}^\mathrm{T}\mathbf{N}dr \tag{A16}$$

$$\mathbf{M}_5 = \sum_{j=1}^{m-1} (\lambda_j + \mu_j) \int_{\Omega_j} \frac{1}{r}\mathbf{W}^\mathrm{T}\mathbf{N}dr + (\lambda_m + \mu_m) \int_{\Omega_m} \frac{\xi}{\tilde{r}}\mathbf{W}^\mathrm{T}\mathbf{N}dr \tag{A17}$$

$$\mathbf{M}_6 = \sum_{j=1}^{m-1} (\lambda_j + 2\mu_j) \int_{\Omega_j} \mathbf{W}^\mathrm{T}\mathbf{N}dr + (\lambda_m + 2\mu_m) \int_{\Omega_m} \xi\mathbf{W}^\mathrm{T}\mathbf{N}dr \tag{A18}$$

$$\mathbf{M}_7 = \sum_{j=1}^{m-1} \mu_j k_{T_j}^2 \int_{\Omega_j} \mathbf{W}^\mathrm{T}\mathbf{N}dr + \mu_m k_{T_m}^2 \int_{\Omega_m} \xi\mathbf{W}^\mathrm{T}\mathbf{N}dr \tag{A19}$$

where, $k_{T_j} = \omega/c_{T_j}$, and c_{T_j} is the shear (torsional) bulk wave velocity of layer Ω_j. Note that the displacement has been discretised in the following way

$$u_q(r) = \sum_{i=1}^{m_q} \mathrm{N}_{qi}(r)u_{qi} = \mathbf{N}_\mathrm{q}\mathbf{u}_\mathrm{q} \tag{A20}$$

where N_{qi} is a global trial (or shape) function, u_{qi} is the value of u_q at node i, and m_q is the number of nodes for the displacements in direction q. In addition, $\mathbf{N}_\mathrm{q}$ and $\mathbf{u}_\mathrm{q}$ are row and column vectors of length m_q, respectively, and it is also convenient to choose $\mathbf{N}_r = \mathbf{N}_\theta = \mathbf{N}_z = \mathbf{N}$. Isoparametric elements are used so that $\mathbf{W} = \mathbf{N}$.

Appendix B

For inner fluid layer Ω_0:

$$\mathbf{R}_{00} = \int_{\Omega_0} \left(\frac{\partial \mathbf{W}_0^T}{\partial r} \frac{\partial \mathbf{N}_0}{\partial r} - \frac{1}{r} \mathbf{W}_0^T \frac{\partial \mathbf{N}_0}{\partial r} + \frac{n^2}{r^2} \mathbf{W}_0^T \mathbf{N}_0 - k_0^2 \mathbf{W}_0^T \mathbf{N}_0 \right) dr \tag{B1}$$

$$\mathbf{R}_{20} = \int_{\Omega_0} \mathbf{W}_0^T \mathbf{N}_0 dr \tag{B2}$$

For outer PML layer Ω_m:

$$\tag{B3}$$

$$\mathbf{R}_{0m} = \int_{\Omega_m} \left(\frac{1}{\xi} \frac{\partial \mathbf{W}_m^T}{\partial r} \frac{\partial \mathbf{N}_m}{\partial r} - \frac{1}{\tilde{r}} \mathbf{W}_m^T \frac{\partial \mathbf{N}_m}{\partial r} + \xi \frac{n^2}{\tilde{r}^2} \mathbf{W}_m^T \mathbf{N}_m - \xi k_m^2 \mathbf{W}_m^T \mathbf{N}_m \right) dr$$

$$\mathbf{R}_{2m} = \int_{\Omega_m} \xi \mathbf{W}_m^T \mathbf{N}_m dr \tag{B4}$$

The pressure has been discretised in the following way:

$$\tilde{p}_j(r) = \sum_{i=1}^{m_j} N_{ji}(r) \tilde{p}_{ji} = \mathbf{N}_j \tilde{\mathbf{p}}_j , j = 0 \text{ or } m \tag{B5}$$

where N_{ji} is a global trial (or shape) function, $\tilde{p}_{ji}$ is the value of $\tilde{p}_j$ at node i, and m_j is the number of nodes (or degrees of freedom) for the pressure in layer Ω_0 or Ω_m. In addition, $\mathbf{N}_j$ and $\tilde{\mathbf{p}}_j$ are row and column vectors of length m_j, respectively, and isoparametric elements are used so that $\mathbf{W} = \mathbf{N}$.

References

1. Lowe MJS, Alleyne DN, Cawley P. Defect detection in pipes using guided waves. Ultrasonics 1998; 36: 147-154.

2. Muggleton JM, Brennan MJ, Pinnington PJ. Wavenumber prediction of waves in buried pipes for water leak detection. Journal of Sound and Vibration 2002; 249: 939-954.

3. Gao Y, Sui F, Muggleton JM, Yang J. Simplified dispersion relationships for fluid-dominated axisymmetric wave motion in buried fluid-filled pipes. Journal of Sound and Vibration 2016; 375: 386-402.

4. Aristégui C, Lowe M.J.S, Cawley P. Guided waves in fluid-filled pipes surrounded by different fluids, Ultrasonics 2001; 39: 367–375.

5. Leinov E, Lowe M.J.S, Cawley P. Investigation of guided wave propagation and attenuation in pipe buried in sand. Journal of Sound and Vibration 2015; 347: 96-114.

6. Leinov E, Lowe M.J.S, Cawley P. Ultrasonic isolation of buried pipes. Journal of Sound and Vibration 2016; 363: 225-239.

7. Benmeddour F, Treyssède F, Laguerre L. Numerical modelling of guided wave interaction with non-axisymmetric cracks in elastic cylinders. International Journal of Solids and Structures 2011; 48: 764-774.

8. Ostachowicz W, Kudela P, Krawczuk M, Zak A, Guided waves in structures for SHM: the time-domain spectral element method. John Wiley & Sons Ltd, UK, 2011.

9. Renno J.M., Mace B. R. Calculating the forced response of cylinders and cylindrical shells using the wave and finite element method. Journal of Sound and Vibration 2014; 333: 5340-5355.

10. Duan W, Kirby R. A numerical model for the scattering of elastic waves from a non-axisymmetric defect in a pipe. Finite Elements in Analysis and Design 2015; 100: 28-40.

11. Duan W, Kirby R, Mudge P. On the scattering of torsional waves from axisymmetric defects in buried pipelines. Journal of the Acoustical Society of America 2017; 141: 3250-3261.

12. Fan D, Lowe M, Castaings M, Bacon C. Torsional waves propagation along a waveguide of arbitrary cross section immersed in a perfect fluid. Journal of the Acoustical Society of America 2008; 124: 2002-2010.

13. Castaings M, Lowe M. Finite element model for waves guided along solid systems of arbitrary section coupled to infinite solid media. Journal of the Acoustical Society of America 2008; 123: 696 – 708.

14. Nguyen KL, Treyssède F, Hazard C. Numerical modeling of three-dimensional open elastic waveguides combining semi-analytical finite element and perfectly matched layer methods. Journal of Sound and Vibration 2015; 344: 158 – 178.

15. P. Zuo, F. Fan. SAFE-PML approach for modal study of waveguides with arbitrary cross-sections immersed in inviscid fluid. Journal of Sound and Vibration 2017; 406: 181 – 196.

16. Duan W, Kirby R, Mudge P, Gan T-H. A one dimensional numerical approach for computing the eigenmodes of elastic waves in buried pipelines. Journal of Sound and Vibration 2016; 384: 177-193.

17. Matuszyk PJ. Modeling of guided circumferential SH and Lamb-type waves in open waveguides with semi-analytical finite element and Perfectly Matched Layer method. Journal of Sound and Vibration 2017; 386: 295-310.

18. Kalkowski M.K., Muggleton M.J., Rustighi E. Axisymmetric semi-analytical finite elements for modelling waves in buried/submerged fluid-filled waveguides. Computers and Structures 2018; 196: 327-340.

19. Hua J, Mu J, Rose JL. Guided wave propagation in single and double layer hollow cylinders embedded in infinite media. Journal of the Acoustical Society of America 2011; 129: 691-700.

20. Astley RJ. Infinite elements for wave problems: A review of current formulations and an assessment of accuracy. International Journal for Numerical Methods in Engineering 2000; 49: 951-976.

21. Hladky-Hennion A-C, Langlet P, de Billy M. Finite element analysis of the propagation of acoustic waves along waveguides immersed in water. Journal of Sound and Vibration 1997; 200: 519-530.

22. Mazzotti M, Marzani A, Bartoli I. Dispersion analysis of leaky guided waves in fluid-loaded waveguides of generic shape. Ultrasonics 2014; 54: 408-418.

23. Mazzotti M, Bartoli I, Castellazzi G, Marzani A. Computation of leaky guided waves dispersion spectrum using vibroacoustic analyses and the Matrix Pencil Method: A validation study for immersed rectangular waveguides. Ultrasonics 2014; 54; 1895-1898.

24. Mazzotti M, Marzani A, Bartoli I. Ultrasonic leaky guided waves in fluid-coupled generic waveguides: hybrid finite-boundary element dispersion analysis and experimental validation. Journal of Applied Physics 2014; 115: 143512.

25. Gravenkamp H, Birk C, Song C. Numerical modelling of elastic waveguides coupled to infinite media using exact boundary conditions. Computers and Structures 2014: 141; 36-45.

26. Gravenkamp H, Birk C, Song C. Computation of dispersion curves for embedded waveguides using dashpot boundary condition. Journal of the Acoustical Society of America 2014: 135: 1127-1138.

27. Gravenkamp H, Birk C, Van J, Modeling ultrasonic waves in elastic waveguides of arbitrary cross-section embedded in infinite solid medium. Computers and Structures 2015: 149; 61-71.

28. Fuller CR, Fahy FJ. Characteristics of wave propagation and energy distributions in cylindrical elastic shells filled with fluid. Journal of Sound and Vibration 1982; 81: 501-518.

29. Komatitsch D, Vilotte J-P; Vai R, Castillo-Covarrubias JM, Sanchez-Sesma FJ, The spectral element method for elastic wave equations – application to 2-D and 3-D seismic problems. International Journal for Numerical methods in Engineering 1999; 45: 1139-1164.

30. Long R, Cawley P, Lowe MJS. Acoustic wave propagation in buried iron water pipes. Proceedings of the Royal Society A: Mathematical, Physical and Engineering Sciences 2003; 459: 2749-2770.

31. Ambrosini RD, Material damping vs. radiation damping in soil–structure interaction analysis. Computers and Geotechnics, 2006; 33 (2): 86-92.